MODERN TRENDS IN PHYSICS RESEARCH

4th International Conference on Modern Trends in Physics Research

MTPR-10

Cairo University, Egypt   12 – 16 December 2010

EDITOR

Lotfia M. El Nadi

Cairo University, Egypt

CONFERENCE PROCEEDINGS ■ VOLUME 9910

Photo-excitation and Photoionization for Plasma Opacities under the Iron Project

Sultana N. Nahar

Department of Astronomy, The Ohio State University, Columbus, OH 43210, USA
E-mail: nahar@astronomy.ohio-state.edu

Opacity gives a measure of radiation transport in a medium such that higher or lower opacity indicates more or less attenuation of radiation. As the radiation propagates, opacity is caused by the absorption and emission of radiation by the constituent elements in the medium, such as astrophysical plasmas. It is also affected by photon scatterings. Hence opacity depends mainly on the intrinsic atomic processes, photo-excitation in a bound-bound transition, photoionization in a bound-free transition, and photon-electron scattering. Monochromatic opacity at a particular frequency, $\kappa(\nu)$, is obtained mainly from oscillator strengths (f) and photoionization cross sections (σ_{PI}). However, the total monochromatic opacity is obtained from summed contributions of all possible transitions from all ionization stages of all elements in the source. Calculation of accurate parameters for such a large number of transitions has been the main problem for obtaining accurate opacities. The overal mean opacity, such as Rosseland mean opacity (κ_R), depends also on the physical conditions, such as temperature and density, elemental abundances and equation of state such as local thermodynaic equilibrium (LTE) of the plasmas. For plasmas under HED (high energy density) conditions, fluid dynamics may be considered for shock waves such as in a supernova explosion.

In this report, I will exemplify the necessity for high precision atomic calculations for the radiative processes of photoexcitation and photoionization in order to resolve some perplexing astrophysical problems relevant to elemental abundances and hence opacities. In particular I will present results on oscillator strengths of Fe XVIII and photoionization cross sections of Fe XVII which are abundant in high temperature plasmas, such as solar corona, and photoionization and recombination of O II which is abundant in low temperature plasmas, such as in a planetary nebula. Sophisticated atomic calculations under the Iron Project are revealing important and dominant features not included in the current opacities. Opacities with these new results are expected to resolve the longstanding problems on abundances in the sun, orion nebula etc.

Keywords: Photoionization; Oscillator strengths; Opacities; Solar and Nebular abundances

1. Introduction

Opacity is a fundamental quantity for studying various quantities such as elemental abundances, physical conditions, stellar pulsations etc of astrophysical and laboratory plasmas. It is used in astrophysical models to obtain internal structure, chemical composition, evolution of states, such as, in local thermodynamic equilibrium (LTE) of the plasmas, etc. As the radiation propagates, it looses energy and slows down by absorption and emission by the constituent elements. The resultant effect is the opacity. Because of opacity the high energy gamma radiation produced by the nuclear fusion in the core of the sun takes over a million years to travel to the surface and escape as optical or low energy photons. Opacity depends on the atomic process of photo-excitations, photoionization and photon scattering.

However, calculation of opacity is quite involved as described in the theory section. For the photon-ion interactions, it depends on the oscillator strengths and photoionization cross sections. Consideration of these processes require large amount of atomic data for all possible radiative transitions. Currently available atomic data for all ions are not accurate and complete enough to compute accurate opacities for various astrophysical problems.

1.1. *The Opacity Project and the Iron Project*

Prior to the Opacity Project (OP),[1,2] there were large discrepancies between astrophysical observations and theoretical predictions obtained using existing opacities for plasmas. These opacities were calculated mainly by Los Alamos National Lab (LANL) using the atomic data obtained from simple approximations. Los Alamos opacities were incorrect by factors of 2 to 5 resulting in inaccurate stellar models. These could not model the Cepheid stars, important to determine distances in astronomy. In response to a plea[3] for accurate opacity from accurate atomic parameters initiated the Opacity Project, an international collaboration of about 25 scientists from 6 countries

Under the OP the first systematic and detailed studies were carried out for the radiative processes of photoexcitation and photoionization for all astro-

physically abundant atoms and ions from hydrogen to iron. Computations were carried out in ab initio close coupling approximation and using R-matrix method. Large amount of atomic data for energy levels, oscillator strengths and photoionization cross sections were obtained. The atomic data are available at data base TOPbase[4] at CDS. New features in photoionization cross sections were revealed. The data were used to calculate the monochromatic opacities and Rosseland mean opacities. The long standing problem on the pulsation ratios of cepheid variables were solved. These atomic data have continued to solve many astrophysical problems. However, a large part of the data are not precise enough for various diagnostics and astrophysical problems.

A follow-up of the OP, the international collaboration of the Iron Project (IP)[5] was initiated to focus on both the radiative and collisional processes, but mainly for the astrophysically abundant iron and iron-peak elements. Work under IP emphasises the relativistic effects and achievement of high accuracy. A new project, RMAX, was also initiated under the IP to focus on the X-ray astrophysics. The large amount of atomic data from the IP are available at TIPbase[6] at CDS, at *Atomic Data and Nuclear Data Tables* and at the NORAD-Atomic-Data site.[7] The monochromatic opacities and Rosseland mean opacities are available at the OPServer[8] at the Ohio Supercomputer Center.

The OP team extended the existing R-matrix codes for radiative processes.[9] The OP results were obtained in nonrelativistic LS coupling approach. In contrast to the OP, IP includes relativistic fine structure effects and the R-matrix method was extended to Breit-Pauli R-matrix (BPRM) method.[10]

Considerable progresses in computational capabilities for higher accuracy are being made under the Iron Project. Higher order relativistic corrections have been added to the BPRM method.[11] Theoretical spectroscopy has been developed for consideration of large number of fine structure levels for all practical purposes.[12,13] This enables calculation of accurate oscillator strengths for larger number of transitions than considered before. We are finding existence of extensive and dominant resonant features in the high energy photoionization cross sections. We have also found important fine structure effects in σ_{PI} in low energy region. We will illustrate results from recent calculations showing more com-

Table 1. A mixture of "standard" solar abundances (10% uncertainties[14]).

Element (k)	Log A_k	A_k/A_H
H	12.0	1.0
He	11.0	1.00(-1)
C	8.55	3.55(-4)
N	7.97	9.33(-5)
O	8.87	7.41(-4)
Ne	8.07	1.18(-4)
Na	6.33	2.14(-6)
Mg	7.58	3.80(-5)
Al	6.47	2.95(-6)
Si	7.55	3.55(-5)
S	7.21	1.62(-5)
Ar	6.52	3.31(-6)
Ca	6.36	2.29(-6)
Cr	5.67	4.68(-7)
Mn	5.39	2.46(-7)
Fe	7.51	3.24(-5)
Ni	6.25	1.78(-6)

plete atomic data and new features. These should facilitate the computation of more accurate monochromatic opacities.

2. Accurate Atomic Data Need

Although data from the OP and IP continue to solve many problems, there are outstanding problems, especially for very high and very low temperature plasmas as discussed below, that remain to be solved. We illustrate the problems in perspectives of the atomic data.

2.1. *High Temperature Plasmas in Solar Corona and Abundances*

The solar elemental abundances are known as: H - 90 % (by number) and 70% (by mass fraction), He - 10 % (by number) and 28 % (by mass), and metals (all elements heavier than helium) - 2% (by mass). In the metals, oxygen is the most abundant and the next ones are C, N, Ne, Mg, Si, S, Fe. The solar abundances are expressed as A_k, usually in log scale. Traditionally H abundance is taken as $\log(A_H) = 12$ and the other elements are scaled relative to it as given in Table 1.

Using the Opacity Project data and mixture of solar elemental abundances given in Table 1, solar opacity were calculated under the OP as shown in Fig. 1.[14] In the figure, there about four bumps or kinks in the curves of various R. They represent
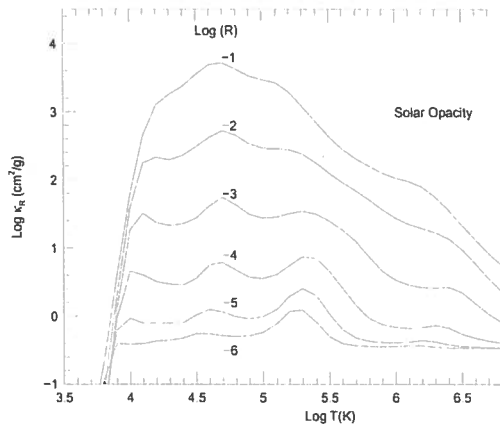
Fig. 1.   Opacities in temperature-density regimes through-out the solar interior. κ is the Rosseland mean opacity and $R = \rho(g\ cc)\ T_6^3$ is the temperature-density parameter with $T_6 = 10^6 K$, i.e. $T_6 = T * 10^{-6}$. For the sun, $-6 \leq R \leq -1$. The four bumps in the curves of various R represent H-, He-, Z-, and inner-shell bumps, that is, higher opacities due to excitation/ionization of the atomic species at those temperatures.[14]

Fig. 2.   Solar interior is defined from the core to the end of the convection zone. At the convection zone plasma bubbles and the radiation escapes.

higher opacities due to excitation/ionization of different atomic species at those temperatures. The first one is the H-bump, the second one is the He-bump, the third one the Z-bump (sum of all elements heavier than H and He) and the fourth one is due to inner-shell excitation/ionization bump. These are general pattern for opacities and are in agreement with the other opacity by OPAL.[15]

However, these do not solve problems that require more presice elemental abundances. For example, the recent determination of solar abundances of light elements, from measurements and 3D hydro NLTE models, show 30-40% lower abundances of C, N, O, Ne, Ar than the standard abundances; these contradict the accurate helioseismology data. One major problem is with the observed and predicted boundary between the solar radiative zine and the convection zone, R_{CZ}. Sun's interior is defined from the - nuclear core to the end of convection zone. At the convection zone plasmas bubble beyond which photons escape. The boundary is known to be accurately measured from helioseismology as 0.713 (relative to the total solar radius, Fig. 2). R_{CZ} can be predicted from opacity through elemental abundances in the solar plasma. The calculated boundary R_{CZ} is 0.726, a much larger value than the measured value. Solar opacity depends on the interior elemental abundances. In the convection zone, the temper-
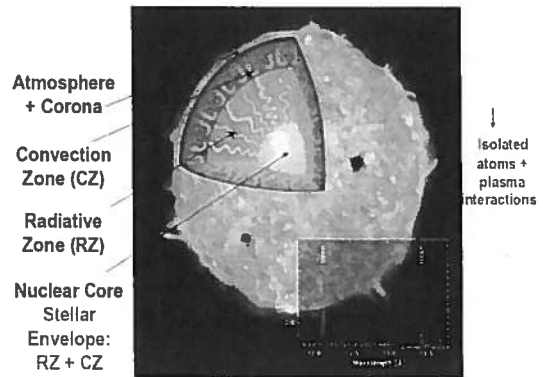
ature is $T_e \sim 193$ eV and the density $n_e \sim 10^{23}/cm^3$ which is a HED (high energy density) condition. At this HED condition, the abundant elements are O, Ne, especially Fe ions in the ionic states of Fe XVII, Fe XVIII, and Fe XIX.

Laboratory set-ups, such as zeta pinch or Z-pinch machines at the Sandia National Lab (SNL) and high power lasers, such as, at National Ignition Facility (NIF), can now study radiation transport or opacity in fusion plasmas. The measurements will enable calibration of the theoretical calculations of basic parameters that govern the opacity. Bailey et al[16] reported achieving HED plasmas at temperature $(T > 10^6$ K) and density $(N > 10^{20}$ cm$^{-3})$ similar to those at the boundary of the solar convection zone. The Z-pinch set-up is a type of plasma confinement system. The plasma is created with laser heating. About 24 Million Amp current is passed through the coil set-ups to generate a gigantic magnetic field that compresses the plasma. The measurement at SNL Z-pinch machine showed that the iron opacity at solar corona is much higher than the prediction obtained using the radiative atomic data, oscillator strengths for photoexcitation and cross sections for photoionization, from the Opacity Project (OP).

2.2. Low Temperature Plasmas and Nebular Abundances

Similar to high temperature plasms, longstanding problems on abundance exists for low temperature astrophysical plasmas, such as, in Orion nebula, planetary nebulae (PNe). A planetary nebula is the last stage of a typical star. Fig. 4 shows PNe K 4-

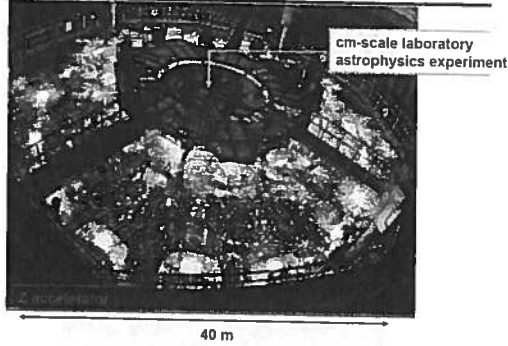cm-scale laboratory astrophysics experiment

40 m

Fig. 3. Magnetically driven z-pinch implosions efficiently convert electrical energy into radiation. Internal shock heating gives out high energy X-rays (1.5 MJ X-rays) with power of aobut ~200 TW.
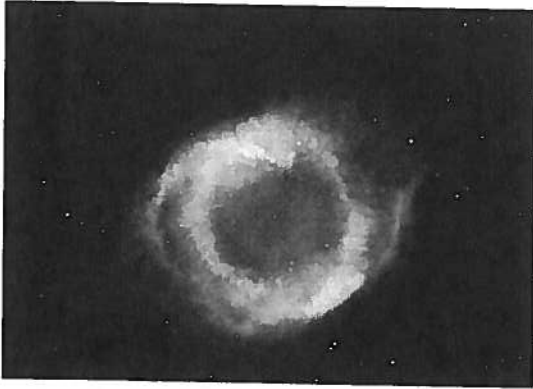

Fig. 4. Planetary nebula Kohoutek 4-55 or K 4-55 by Hubble Space Telescope. The envelope of thin gas is illuminated by the radiation from the hot central core.

55 nearly 4,600 light-years away in the constellation Cygnus. The condensed central star is at very high temperature of about T~100,000 K whereas for a typical star T≤ 40,000 K. The envelope of a PNe is thin gas formed by the radiatively ejected gas by the star and is illuminated by the radiation from the central star.

The cooler envelope is rich in elements, such as, oxygen, nitrogen, at low ionization stages. Lines of O III and O II are detected indicating low density and low temperature. At very low densities, electrons can populate excited metastable energy levels which on de-excitation gives lines, often fobidden ones. Abundance can be obtained from these lines due to collisional excitation. At low temperature, electrons combine with the ions by giving out photons which form the recombination lines. These lines also give abundance of the element. However, there is a discrep-

ancy between abundances of oxygen calculated from collisionally excited lines (CEL) of O III Lines and from the recombination lines (REL) from O III to O II. The former is larger than the latter, that is, $N_e N(O\ III)\alpha_R(T) < N_e N(O\ III)q_{EIE}(T)$ and has been a puzzle for many years. One solution for the problem would be to have predicted recombination rate for O III→O II is higher than that at the present time.

3. Photo-excitation, Photoionization and Opacity

Opacity $\kappa(\nu)$ depends on oscillator strengths of photoexcitation. Photo-excitation and de-excitation can be described as

$$X^{+Z} + h\nu \rightleftharpoons X^{+Z*}$$
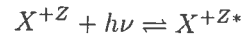
where X^{+Z} is the ion with charge Z. The emitted or absorbed photon ($h\nu$) is observed as a spectral line. The relevant atomic parameters for the direct and inverse processes are oscillator strength (f) and radiative decay rate (A-value). f_{ij} is related to $\kappa(\nu)$ as

$$\kappa_\nu(i \rightarrow j) = \frac{\pi e^2}{mc} N_i f_{ij} \phi_\nu \qquad (1)$$

N_i is the ion density in state i, ϕ_ν is a profile factor which can be Gaussian, Lorentzian, or combination of both over a small wavelength range.

The other radiative process that determines opacity is photoionization when an electron is ejected with absorption of a photon,

$$X^{+Z} + h\nu \rightleftharpoons X^{+Z+1} + \epsilon$$
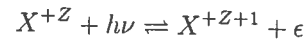
The inverse process is radiative recombination (RR) when an electron recombines to an ion with emission of a photon. These can occur via an intermediate doubly excited state as:

$$e + X^{+Z} \rightleftharpoons (X^{+Z-1})^{**} \rightleftharpoons \begin{cases} e + X^{+Z} & \text{AI} \\ X^{+Z-1} + h\nu & \text{DR} \end{cases}$$
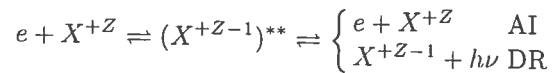
A colliding electron excites the target and attaches to form the short-lived doubly excited autoionizing state. The state leads either to autoionization (AI) where the electron goes free and target drops to ground state or to dielectronic recombination (DR) where the electron gets bound by emission of a photon. The autoionizing state manifests as an enhancement or resonance in the process. Photoionization resonances can be seen in absorption spectra while

recombination resonances can be seen in emission spectra. The atomic parameters for these processes correspond to photoionization cross sections (σ_{PI}) and recombination rates. $\kappa(\nu)$ for photoionization is obtained from σ_{PI} as

$$\kappa_\nu = N_i \sigma_{PI}(\nu) \tag{2}$$

κ_ν depends also on two other processes, inverse Bremsstrahlung or free-free (ff) scattering and photon-electron scattering. Bremsstrahlung refers to the radiation emitted by a charged particle accelerated in an electromagnetic field. The inverse process is where a free electron and an ion can absorb a photon in free-free interaction, that is,

$$h\nu + [X_1^+ + e(\epsilon)] \rightarrow X_2^+ + e(\epsilon') \tag{3}$$

Explicit calculations for the free-free scattering cross sections may be done using the elastic scattering matrix elements for electron impact excitation of ions. An approximate expression for the free-free opacity is given by

$$\kappa_\nu^{ff}(1\ 2) = 3\ 7 \times 10^8 N_e N_i g_{ff} \frac{Z^2}{T^1\ ^2 \nu^3} \tag{4}$$

where g_{ff} is a Gaunt factor.

The photon electron scattering can be of two type, Thomson scattering, when the electron is free and Rayleigh scattering when the electron is bound to an atomic or molecular species. κ is related to Thomson scattering cross section σ^{Th},

$$\kappa(sc) = N_e \sigma^{Th} = N_e \frac{8\pi e^4}{3m^2 c^4} = 6\ 65 \times 10^{-25}\ cm^2\ g \tag{5}$$

To Rayleigh scattering cross section σ^R, opacity is related as

$$\kappa_\nu^R = n_i \sigma_\nu^R \approx n_i f_t\ \sigma^{Th} \left(\frac{\nu}{\nu_I} \right)^4 \tag{6}$$

where n_i is the density of the atomic or molecular species, $h\nu_I$ is the binding energy and f_t is the total oscillator strength associated with the bound electron, i.e. the sum of all possible transitions, such as the Lyman series of transitions $1s \rightarrow np$ in hydrogen.

To find the average opacity, such as Rosseland opacity, we need elemental abundances. These are obtained from proper equation of state (EOS) which gives the ionization fractions and level populations of each ion of an element in levels with non-negligible occupation probability. For example, for plasmas in local thermodynamic equilibrium (LTE) Saha equation is the EOS. However, Saha equation is not applicable in non-LTE condition. Some details of the opacity calculations can be found in.[17] The average opacity also depends on the physical condition of the plasmas, such as, the density and temperature

Rosseland mean opacity $\kappa_R(T\ \rho)$ is the harmonic mean opacity averaged over the Planck function, $g(u)$,

$$\frac{1}{\kappa_R} = \frac{\int_0^\infty \frac{1}{\kappa_\nu} g(u) du}{\int_0^\infty g(u) du} \tag{7}$$

where $g(u)$ is given by

$$g(u) = \frac{15}{4\pi^4} \frac{u^4 e^{-u}}{(1 - e^{-u})^2} \quad u = \frac{h\nu}{kT} \tag{8}$$

$g(u)$, for an astrophysical state is calculated with different chemical compositions H (X), He (Y) and metals (Z), such that

$$X + Y + Z = 1 \tag{9}$$

4. Theoretical Approach

4.1. Breit-Pauli R-matrix Method

We use the Breit-Pauli R-matrix (BPRM) method to calculate the oscillator strengths and photoionization cross sections. It uses close coupling approximation for the wave function. The relativistic Breit-Pauli Hamiltonian is given by

$$H^{BP} = H^{NR} + H^{mass} + H^{Dar} + H^{so} +$$

$$\frac{1}{2} \sum_{i \neq j}^N [g_{ij}(so + so') + g_{ij}(ss') + g_{ij}(css') +$$

$$g_{ij}(d) + g_{ij}(oo')] \tag{10}$$

H^{NR} is the nonrelativistic Hamiltonian,

$$H^{NR} = \sum_{i=1}^N \left\{ -\nabla_i^2 - \frac{2Z}{r_i} + \sum_{j>i}^N \frac{2}{r_{ij}} \right\} \tag{11}$$

and the one-body relativistic correction terms are mass correction, Darwin and spin-orbit interaction terms respectively,

$$H^{mass} = -\frac{\alpha^2}{4} \sum_i p_i^4 \quad H^{Dar} = \frac{\alpha^2}{4} \sum_i \nabla^2 \left(\frac{Z}{r_i} \right)$$

$$H^{so} = \left[\frac{Ze^2 \hbar^2}{2m^2 c^2 r^3} \right] \tag{12}$$

The spin-orbit interaction H^{so} splits LS energy in to fine structure levels. Rest of the terms are two-body interaction terms where the notation are s for spin and a prime indicates 'other', o for orbit, c for contraction, and d for Darwin. These terms are much weaker but can become important for weak transitions and when relativistic effects are important.

BPRM method[5,10] included the three one-body relativistic correction terms in the Hamiltonian:

$$H^{BP}_{N+1} = H^{NR}_{N+1} + H^{mass}_{N+1} + H^{Dar}_{N+1} + H^{so}_{N+1} \qquad (13)$$

Inclusion of two-body interaction terms are much for complicated. The first two two-body terms provide the Breit interaction

$$H^B = \sum_{i>j} [g_{ij}(so + so') + g_{ij}(ss')] \qquad (14)$$

where

$$g_{ij}(so + so') = -\alpha^2 [(\frac{\mathbf{r}_{ij}}{r_{ij}^3} \times \mathbf{p}_i)\,(\mathbf{s}_i + 2\mathbf{s}_j) +$$

$$(\frac{\mathbf{r}_{ij}}{r_{ij}^3} \times \mathbf{p}_j)\,(\mathbf{s}_j + 2\mathbf{s}_i)] \qquad (15)$$

$$g_{ij}(ss') = 2\alpha^2 \left[\frac{\mathbf{s}_i\,\mathbf{s}_j}{r_{ij}^3} - 3\frac{(\mathbf{s}_i\,\mathbf{r}_{ij})(\mathbf{s}_j\,\mathbf{r}_{ij})}{r_{ij}^5} \right] \qquad (16)$$

which contributes more relatively to the other terms. In the latest development of the BPRM codes, Breit interaction has been included.[11]

In close coupling (CC) approximation, the wave function is represented by an expansion where the ion is treated as a system of (N+1) electrons. The core ion, termed as the target, has N electrons and the additional electron is the interacting (N+1)th electron. The total wave function expansion is expressed as:

$$\Psi_E(e + ion) = A \sum_i^N \chi_i(ion)\theta_i + \sum_j c_j \Phi_j(e + ion) \qquad (17)$$

where χ_i is the target ion or core wave function which includes excitations. θ_i is interacting electron wave function (continuum or bound), and Φ_j is a correlation function of (e+ion). The complex resonant structures in the atomic processes are included through coupling of bound and continuum channels with core excitations. The target wave functions χ_i are obtained from atomic structure calculations, e.g. SUPERSTRUCTURE (SS),[18,19]

Substitution of $\Psi_E(e + ion)$ in $H\Psi_E = E\Psi_E$ results in a set of coupled equations which are solved
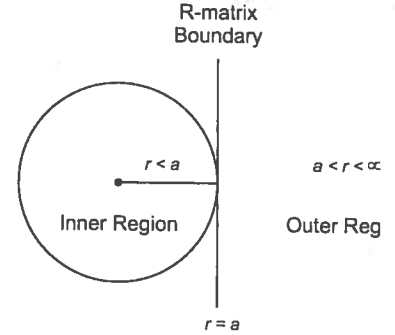

Fig. 5. In R-matrix method, the space is divided into two regions, the inner and the outer regions, of a sphere of radius r_a with the ion at the center.

by the R-matrix method. In the R-matrix method (Fig. 5), the space is divided in two regions, the inner and the outer regions, of a sphere of radius r_a with the ion at the center. r_a, the R-matrix boundary, is chosen large enough for electron-electron interaction potential to be zero outside the boundary. The wave function at $r > r_a$ is Coulombic due to perturbation from the long-range multipole potentials. In the inner region, the partial wave function of the interacting electron is expanded in terms of a basis set, called the R-matrix basis, $F_i = \sum a_k u_k$, which satisfy

$$\left[\frac{d^2}{dr^2} - \frac{l(l+1)}{r^2} + V(r) + \epsilon_{lk} \right] u_{lk} + \sum_n \lambda_{nlk} P_{nl}(r) = 0$$

$$(18)$$

and are made continuous at the boundary by matching with the Coulomb functions outside the boundary. For negative energy, the solution is a bound (e+ion) states, Ψ_B and for positive energy, the solution is a continuum state, Ψ_F.

4.2. Atomic Quantities

To calculate oscillator strengths and photoionization cross sections, we obtain the line strength first. It depends on the transitions matrix element for the bound-bound (photoexcitation) and bound-free (photoionization) transitions with a dipole operator. The dipole transition matrix elements for photoexcitation and photoionization are

$$< \Psi_B \ \mathbf{D} \ \Psi_{B'} > \quad < \Psi_B \ \mathbf{D} \ \Psi_F > \qquad (19)$$

respectively, where $\mathbf{D} = \sum_i \mathbf{r}_i$ is the dipole operator and and the sum is over the number of electrons.

The reduced tensor $\mathbf{D}$ gives 3-j symbols for angular momenta on simplification. The transition matrix element reduces to generalized line strength as

$$S = \left| \left\langle \Psi_f \sum_{j=1}^{N+1} r_j \Psi_i \right\rangle \right|^2 \qquad (20)$$

This is the quantity of interest for both the processes.

The oscillator strength (f_{ij}) and radiative decay rate (A_{ji}) for the bound-bound transition are obtained as

$$f_{ij} = \left[\frac{E_{ji}}{3g_i} \right] S \quad A_{ji}(sec^{-1}) = \left[0\,8032 \times 10^{10} \frac{E_{ji}^3}{3g_j} \right] S \qquad (21)$$

The photoionization cross section, σ_{PI}, is obtained as

$$\sigma_{PI} = \left[\frac{4\pi}{3c} \frac{1}{g_i} \right] \omega S \qquad (22)$$

where ω is the incident photon energy in Rydberg unit.

With consideration of relativistic fine structure effects, BPRM method enables extensive sets of E1 transitions (Δ j=0,±1, $\Delta L = 0, \pm 1, \pm 2$, parity π changes) with same spin-multiplicity ($\Delta S = 0$) and intercombination ($\Delta S \neq 0$). On the contrary LS coupling allows only same spin-multiplicity transitions.

Large sets of various forbidden transitions are considered in Breit-Pauli approximation using atomic structure calculations. Due to small f-values, typically the radiative decay rates, A−values, are calculated for the forbidden transitions. These transitions are mainly i) electric quadrupole (E2) transitions (Δ J = 0,±1,±2, parity does not change)

$$A_{ji}^{E2} = 2\,6733 \times 10^3 \frac{E_{ij}^5}{g_j} S^{E2}(i\ j)\ s^{-1} \qquad (23)$$

ii) magnetic dipole (M1) transitions (Δ J = 0,±1, parity does not change),

$$A_{ji}^{M1} = 3\,5644 \times 10^4 \frac{E_{ij}^3}{g_j} S^{M1}(i\ j)\ s^{-1} \qquad (24)$$

iii) electric octupole (E3) transitions (Δ J= ±2, ±3, parity changes) and

$$A_{ji}^{E3} = 1\,2050 \times 10^{-3} \frac{E_{ij}^7}{g_j} S^{E3}(i\ j)\ s^{-1} \qquad (25)$$

iv) magnetic quadrupole (M2) transitions (Δ J = ±2, parity changes) and

$$A_{ji}^{M2} = 2\,3727 \times 10^{-2} s^{-1} \frac{E_{ij}^5}{g_j} S^{M2}(i\ j) \qquad (26)$$

Some details of the forbidden transitions are given in.[19,20] These transitions are treated through atomic structure code SUPERSTRUCTURE[18] and its later version.[19]

With the A-values, the lifetime of a level can be obtained easily as,

$$\tau_k(s) = \frac{1}{\sum_i A_{ki}(s^{-1})} \qquad (27)$$

5. Results and Discussions

The accuracy and completeness of oscillator strengths for bound-bound transitions and new features in photoionization affecting the plasma opacities are discussed with examples in subsections below.

5.1. *Energy Levels and Oscillator Strengths*

Iron is a dominant metal and astrophysical spectra are rich with its lines. However, due to strong electron-electron correlations, it is a computational challenge to compute accurate atomic data for various ionic states of iron. One objective of the Iron Project is to study systematically the energy levels and lines of various ion ions. A few examples of the iron ions for which accurate and complete data for oscillator strengths are available for all practical needs are Fe XVII,[19] Fe XVIII,[21] Fe XIX[22] which are abundant in solar corona.

The large number of energy levels and transitions that BPRM method can compute are identified spectroscopically through a major task of many tests. It is different from atomic structure calculations where identification of an energy level is based on the percentage contributions of the configurations. In BPRM method, such contributions can not be obtained. Identification is carried out with a method developed based on the channel contributions in the outer region of the R-matrix method, quantum defect theory, and algebraic algorithms.[12,13] The identified levels match with those from atomic structure calculations for most cases. However, since BPRM considers larger number of configurations causing more mixing coefficients and quantum defects are often too close to differentiate for closely lying levels, identifications may differ. The difference also depends on the set of the configurations selected and the way configurations are optimized.

Table 2. Sample set of fine structure energy levels of Fe XVIII.[21] The levels are grouped as sets of LS term components. C_t is the core configuration, ν is the effective quantum number.

$C_t(S_tL_t\pi_t)$	J_t	nl	$2J$	E(Ry)	ν	$SL\pi$
Eqv electron/unidentified levels, parity: o						
2s22p5			3	-9.98779E+01	0.00	2P o
2s22p5			1	-9.89033E+01	0.00	2P o
Nlv(c)= 2 : set complete						
Eqv electron/unidentified levels, parity: e						
2s22p5			1	-9.00863E+01	0.00	2S e
Nlv(c)= 1 : set complete						
Nlv= 3, $^4L^e$: P (5 3 1)/2						
2s22p4	(3Pe)	2 3s	5	-4.30858E+01	2.74	4P e
2s22p4	(3Pe)	2 3s	3	-4.28383E+01	2.75	4P e
2s22p4	(3Pe)	0 3s	1	-4.23704E+01	2.74	4P e
Nlv(c)= 3 : set complete						
Nlv= 2, $^2L^e$: P (3 1)/2						
2s22p4	(3Pe)	1 3s	3	-4.21961E+01	2.74	2P e
2s22p4	(3Pe)	1 3s	1	-4.19680E+01	2.75	2P e
Nlv(c)= 2 : set complete						
Nlv= 2, $^2L^e$: D (5 3)/2						
2s22p4	(1De)	2 3s	5	-4.14059E+01	2.75	2D e
2s22p4	(1De)	2 3s	3	-4.13716E+01	2.75	2D e
Nlv(c)= 2 : set complete						
Nlv= 8, $^4L^o$: S (3)/2 P (5 3 1)/2 D (7 5 3 1)/2						
2s22p4	(3Pe)	2 3p	3	-4.08315E+01	2.82	4SPD o
2s22p4	(3Pe)	2 3p	5	-4.07910E+01	2.82	4PD o
2s22p4	(3Pe)	2 3p	1	-4.05398E+01	2.83	4PD o
2s22p4	(3Pe)	2 3p	7	-4.04861E+01	2.83	4D o
2s22p4	(3Pe)	2 3p	5	-4.04822E+01	2.83	4PD o
2s22p4	(3Pe)	0 3p	1	-4.00221E+01	2.82	4PD o
2s22p4	(3Pe)	0 3p	3	-3.98416E+01	2.83	4SPD o
2s22p4	(3Pe)	0 3p	3	-3.96589E+01	2.83	4SPD o
Nlv(c)= 8 : set complete						

Table 3. Comparison of calculated BPRM absolute energies, E_c, of Fe XVIII[21] with observed values, E_o, compiled by NIST.[7] I_J is the level index for the calculated energy position in symmetry $J\pi$. The asterisk next to a J-value indicates that the term has missing fine structure components in the observed set.

Level		$J : I_J$	E_a(Ry)	E_r(Ry)
2s22p5	$^2P^o$	1.5 :1	9.98779E+01	1.00100E+02
2s22p5	$^2P^o$	0.5 :1	9.89033E+01	9.91652E+01
2s2p6	^2S	0.5 :1	9.00863E+01	9.03977E+01
2s22p4(3P)3s	^4P	2.5 :1	4.30858E+01	4.34010E+01
2s22p4(3P)3s	^4P	1.5 :1	4.28383E+01	4.25270E+01
2s22p4(3P)3s	^4P	0.5 :2	4.23704E+01	4.25972E+01
2s22p4(3P)3s	^2P	1.5 :2	4.21961E+01	4.31631E+01
2s22p4(3P)3s	^2P	0.5 :3	4.19680E+01	4.23020E+01
2s22p4(1D)3s	^2D	2.5 :2	4.14059E+01	4.17789E+01
2s22p4(1D)3s	^2D	1.5 :3	4.13716E+01	4.17413E+01
2s22p4(1S)3s	^2S	0.5 :4	3.99754E+01	4.01833E+01
2s22p4(3P)3d	^4P	2.5 :3	3.77130E+01	3.71888E+01
2s22p4(3P)3d	^4P	1.5 :4	3.76699E+01	3.74741E+01
2s22p4(3P)3d	^4P	0.5 :5	3.75811E+01	3.76035E+01
2s22p4(3P)3d	^2F	2.5*:4	3.70202E+01	3.74012E+01
2s22p4(3P)3d	^4D	1.5*:5	3.70925E+01	3.70494E+01
2s22p4(3P)3d	^4D	0.5*:6	3.72334E+01	3.71934E+01
2s22p4(3P)3d	^2P	1.5*:6	3.68203E+01	3.67915E+01
2s22p4(3P)3d	^2D	2.5*:6	3.65122E+01	3.67031E+01
2s22p4(1D)3d	^2S	0.5 :7	3.57466E+01	3.61810E+01
2s22p4(1D)3d	^2P	1.5 :9	3.55279E+01	3.59614E+01
2s22p4(1D)3d	^2P	0.5 :8	3.51835E+01	3.56351E+01
2s22p4(1D)3d	^2D	2.5 :8	3.57466E+01	3.59395E+01
2s22p4(1D)3d	^2D	1.5 :10	3.52693E+01	3.57080E+01

For example, for Fe XVIII BPRM method produced 1174 fine structure levels with $n \leq 10$ and $l \leq 9$[21] compared to available observed 66 levels (NIST compiled table[23]). The calculated levels are identified and are checked for completeness as shown for Fe XVIII in the Table 2. The top line for each set of energy levels shows total number of possible levels (Nlv) with LS states and corresponding J values. The last column of the set gives the possible LS state with fixed spin multiplicity and parity.

The calculated BPRM energies are of high accuracy agreeing with the most accurate and measured values by a few percent. For Fe XVIII levels, the agreement is within 1% for most levels, the highest discrepancy being 3%. Table 3 shows comparison of Fe XVIII energies with the measured values of Shirai et al[7] listed in NIST[23] compilation.

The bound levels of Fe XVIII with $n \leq 10$ correspond to 141,869 allowed electric dipole transitions over a broad energy range. The accuracy of these transitions are made with the limited number of available transitions, particularly with those evaluated and compiled by the NIST. The available values are obtained from atomic structure calculations by various investigators and are in good agreement of the BPRM values in general. It may be noted that the evaluated accuracies by NIST are not necessarily consistent with the agreement between BPRM radiative decay rates and other calculations. Table 4 presents comparison of radiative decay rates (A-values) and good agreements can be seen between BPRM and other values. A single measurement of lifetime of level $2s2p^5(^3P_2^o)$ is also in good agreement with the BPRM value.

The IP considers the forbidden transitions mainly for diagnostics and collisional modeling. Because of weaker in nature forbidden transitions are considered up to $n \leq 5$ in general and are obtained through atomic structure calculations. Nahar[21] reported forbidden transitions of Fe XVIII of type electric (E2, E3) and magnetic (M1, M2) multipoles up to n=4, that is, up to $4f$ with a total of 29,682 transitions. They are from 243 fine structure levels of fifteen configurations. Comparison of these levels with the measured values (NIST compilation) shows

agreement within 1% for most levels. The largest difference is 3.4% for the level $2s2p^5(^1P^o)3p\,^2D$. Comparison of forbidden transitions is also made in Table 4 showing good agreement with others.

Table 4. Comparison of present radiative decay rates, A-values, (in units of s^{-1}) for Fe XVIII with those from previous calculations. The letter in the second column gives NIST accuracy rating. Notation $a + b$ means $a \times 10^b$.

λ Å	A:Ac Others	A Present	$C_i - C_j$	$SL\pi$ i-j	g i-j
			E1		
93.926	9.13+10^a:C$^+$	7.75+10	$2s22p5 - 2s2p6$	$^2P'' - ^2S$	4-2
103.94	3.31+10^a:C$^+$	2.81+10	$2s22p5 - 2s2p6$	$^2P'' - ^2S$	2-2
15.766	1.4+12^{a,b}:D	1.16+12	$2s^22p^5 - 2s^22p^4\,^3P3s$	$^2P'' - ^2P$	4-2
16.026	1.5+12^{a,b}:D	1.34+12	$2s^22p^5 - 2s^22p^4\,^3P3s$	$^2P'' - ^2P$	2-2
15.847	2.0+11^a:E	1.88+11	$2s^22p^5 - 2s^22p^4\,^3P3s$	$^2P'' - ^4P$	4-2
16.072	9.1+10^a:E	8.44+10	$2s^22p^5 - 2s^22p^4\,^3P3s$	$^2P'' - ^4P$	4-6
15.625	1.1+12^{a,b}:D	9.68+11	$2s^22p^5 - 2s^22p^4\,^1D3s$	$^2P'' - ^2D$	4-6
15.870	1.3+12^{a,b}:D	1.19+12	$2s^22p^5 - 2s^22p^4\,^1D3s$	$^2P'' - ^2D$	2-4
14.152	4.3+12^{a,b}:E	3.55+12	$2s^22p^5 - 2s^22p^4\,^1D3d$	$^2P'' - ^2D$	4-4
14.361	1.5+13^{a,b}:E	1.33+13	$2s^22p^5 - 2s^22p^4\,^1D3d$	$^2P'' - ^2D$	2-4
14.203	1.9+13^{a,b}:E	1.83+13	$2s^22p^5 - 2s^22p^4\,^1D3d$	$^2P'' - ^2P$	4-4
14.418	3.2+12^{a,b}:E	2.61+12	$2s^22p^5 - 2s^22p^4\,^1D3d$	$^2P'' - ^2P$	2-4
15.209	2.8+11^b:E	2.09+11	$2s^22p^5 - 2s^22p^4\,^1S3s$	$^2P'' - ^2S$	4-2
13.919	9.6+10^b:E	5.32+10	$2s^22p^5 - 2s^22p^4\,^1S3d$	$^2P'' - ^2D$	4-4
13.954	1.1+12^{a,b}:D	9.94+11	$2s^22p^5 - 2s^22p^4\,^1S3d$	$^2P'' - ^2D$	4-6
14.121	1.5+13^{a,b}:D	1.32+13	$2s^22p^5 - 2s^22p^4\,^1S3d$	$^2P'' - ^2D$	2-4
			E2,M1		
974.86	1.9+00^{a,b}:D	1.98	$2s^22p^5 - 2s^22p^5 : E2$	$^2P'' - ^2P''$	4-2
974.86	1.93+04^a:C	1.94+04	$2s^22p^5 - 2s^22p5 : M1$	$^2P'' - ^2P''$	4-2

λ	Lifetime ($10^{-12}s$) Expt	Present	$C_i - C_j$	$SL\pi$ i-j	g i-j
93.9	12.2±0.8^c	12.90	$2s22p5 - 2s2p6$	$^2P'' - ^2S$	4-2

a - Cheng et al. 1979, b - Fawcett 1984, c - Buchet et al 1980

The effect of accuracy on opacities was tested for Fe IV by Nahar and Pradhan[?] with more improved oscillator strengths than that obtained earlier under the OP. The oscillator strengths were processed for fine structure splittings, but with no relativistic corrections. They obtained monochromatic opacities for Fe IV at a temperature logT(K)=4.5 and electron density $\log N_e(\text{cm}^{-3}) = 17.0$, where Fe IV dominates the iron opacity. They found that κ_ν which depends primarily on oscillator strengths, differs considerably from those obtained using earlier oscillator strengths of the OP as shown in Fig. 6. κ_ν varies over orders of magnitude between 500 - 4000 Å. Comparison in-
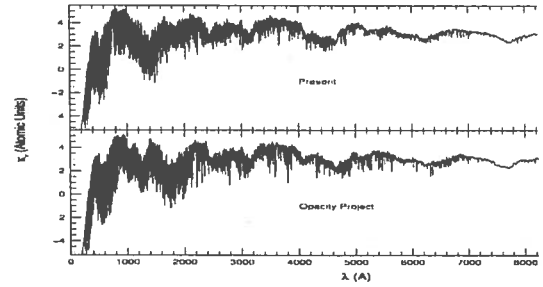
dicates systematic shift in groups of OP energies.

Fig. 6. Monochromatic opacities (κ_ν) of Fe IV using atomic transitions from the Opacity Project in TOPbase (lower panel) and using data from later calculations under the Iron Project[28] showing considerable differences, especially in region of 500 - 4000 Å

5.2. Photoionization

Opacity is caused by photoionization, but mainly through the photon absorption at resonant energies. The resonances are introduced as the core goes through excitations. The OP work computed the resonances in photoionzation of the ground and many excited states of many atomic systems for the first time. However, the work focused only the low energy resonances. It was assumed that low energy resonances due to couplings of channels with the lower excitations of the core ion are more dominant. However, later investigations under the IP revealed that resonances due to excitations of the high lying core states of ions, such as for Fe XXI, could play a very important role for cases, such as Fe XXI[29]).

Relativistic fine structure effects at low energy can also reveal structures which are not allowed in LS coupling approximation (e.g. for Fe XXI[29]). These structures, not studied before, can be very important for low temperature plasmas where they will change the current calculated opacities and expect to resolve or reduce large gaps of differences between the observational and calculated values. These new features are illustrated in the following two sections.

5.2.1. High Energy Photoionization

High energy photoionization is important for high temperature plasmas where elements can be in highly ionized states. It is usually assumed that high energy photoionization is featureless and decays similar to that of a hydrogenic ion. It is also a computational

challenge to get cross section over a great energy range. Nonetheless, it is highly crucial to study the high energy photoionization features which can be much more prominent than those of low temperature.

We have recently completed the computations for photoionization cross sections (σ_{PI}) for Fe XVII[30] using the BPRM method. In addition to solar corona, this ion is abundant in high temperature plasmas of many other astronomical objects. This is the first ion for which high energy photoionization has been studied using the BPRM method. The energy diagram for core excitations of this ion gives an image of typical resonant strucutes in a relatively small energy range beyond the ionization threshold. The core ion, Fe XVIII, has three levels in the n=2 complex beyond which there is a large energy gap of about 47 Ry before the core can be excited to n=3 levels. Our computation included 60 levels of n=2 and n=3 complexes of Fe XVIII. Earlier calculations assumed that the very high lying n=3 levels have small coupling effects on photoinization.

It is known that the n=3 excitations do not form any bound state of Fe XVII. The n=3 core levels lie too high above to form any bound level. The recent study[30] finds that although n=3 core excitations do not form any bound state, they form autoionizing states and appear as strong resonances in photoionization cross section as shown in Fig. 7. Most of these resonances are Rydberg series autoionizing resonances. They form at energies E_p,

$$(E_t - E_p) = z^2 \ \nu^2$$

where E_t is an excited core state or threshold and ν is the effective quantum number of the state. Each excited core state corresponds to a Rydberg series although the resonances may not be prominent for the some states. These resonances are usually narrow and more common. The autoionizing states of n=3 levels do not have much impact, except appearing as some weak resonances, on the ground level σ_{PI} as seen in the top panel of Fig. 7. The figure present σ_{PI} of the a) ground level $2s^2 2p^6 (^1S_0)$ and b) an excited level $2s^2 2p^5 3d(^3P_0^o)$ of Fe XVII. In the figure arrows point energy limits of n=2 and 3 core states. While resonances introduced by the core excitations to n=2 levels are important for the ground level, excitations to n=3 levels are more important for the excited level photoionization. The high energy region of σ_{PI} of the
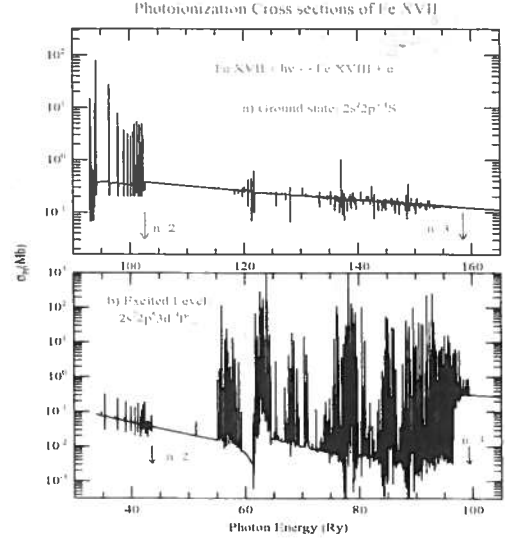

Fig. 7. Photoionization cross section σ_{PI} of Fe XVII. For the ground level: n=2 resonances are important and for an excited level: n=3 resonances are important. Arrows point energy limits of n=2 and 3 core states.

excited level is filled with high peak resonances.

The wide PEC (photo-excitation-of-core) or Seaton resonances in the high energy region are the other dominant contributors to plasma opacity. These resonances occur when the core goes through a dipole allowed transition while the outer electron remains as a spectator. The state is followed by ionization via the outer electron while the core drops down to the ground state. The ground level of core Fe XVIII is $2s^2 2p^5(^2P_{3/2}^o)$. Hence a PEC resonance can form when the core goes through the dipole transition, $2s^2 2p^5(^2P_{3/2}^o) - 2s^2 2p^4 3s(^2P_{3/2})$. PEC resonances are manifested at the excited energy threshold that the core was excited to. PEC resonances exist in valence electron excited states only, that is, no PEC resonance for the ground or equivalent electron states. The resonant phenomena was first explained by Seaton in.[31] Fig. 8 presents σ_{PI} of the excited level, $2s^2 2p^5 7f(^3D_1)$, of Fe XVII. The present calculations includes 29 possible dipole allowed transitions for the core ground level and each corresponds to a Seaton resonance. The overlapping Seaton resonances have been pointed by couple of arrows in the figure. As the figure shows, Seaton resonances are strong which increase the background cross sections by orders of magnitude. The shape and strength of
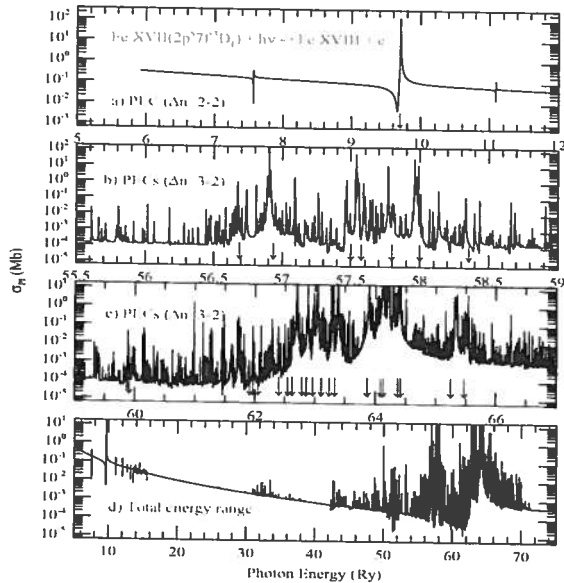
Fig. 8. Photoionization cross section (σ_{PI}) of excited level $2p^37f(^3D_1)$ over various ranges of energy (a,b,c) while the bottom panel (d) presents the total range. PEC resonances appear, positions pointed by arrows, occur at energies of dipole transitions in the core. They are high-peak, wider and enhance the background σ_{PI} by orders of magnitude, and will affect photoionization and recombination rates, especially of high temperature plasmas.

Fig. 9. Comparison of photoionization cross section (σ_{PI}) of excited levels $2p^37f(^3D_1)$. PEC resonances appear at energies of core dipole transitions. They are strong & enhance the background σ_{PI} by orders of magnitude. Will affect photoionization & recombination rates of high temperature plasmas

PEC resonances depend on the interference of core excitations and overlapping Rydberg series of resonances. These dominating features, especially those due to Δn =3-2 core transitions, show large enhancement of photon absorptions related to the opacities. These are non-existent in the available data and thereby grossly underestimating the opacity.

Photoionization cross sections of two levels of Fe XVII obtained from BPRM calculations and from the OP are compared in Fig. 9. Panels (a,b) shows σ_{PI} of level $2p^53p^1P$ and panels (c,d) of level $2p^53d(^1D^o)$, respectively. Comparison shows low and smooth background in OP cross sections in panels (a) and (c) while BPRM σ_{PI}? filled with resonant structures. These high peak resonances in BPRM cross section indicate higher probability of photoionization. Without inclusion of n=3 core states, σ_{PI} is considerably underestimated. These resonances also indicate higher absorption of photons by orders of magnitude. These will increase opacity which currently include only Δ n=2-2 core excitation.
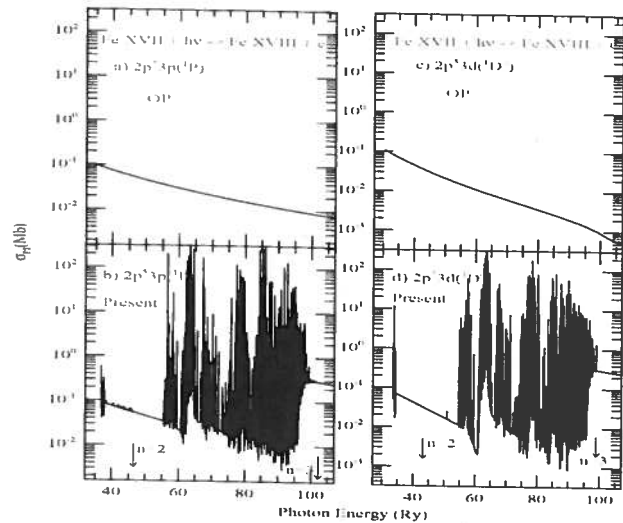
5.2.2. Low Energy Photoionization

Relativistic effects are not significant for low to medium Z elements for most practical applications. Hence photoioniation cross sections calculated in LS coupling can be of high accuracy to benchmark experimental measurement with very good agreement. However, there are cases when resonant features are formed by the allowed fine structure coupling, but not allowed in LS coupling, in the very low energy region and are of crucial importance.

An example of such a case is photoionization of O II. Importance of O II as a diagnostic element is well known for the low temperature plasmas in Orion nebula from where its lines can be observed as mentioned above. The radiative and collisional processes of O II are well studied and accurate parameters for the processes are available. The experimental measurement of the O II photoionization at the high resolution set-up of ALS (Advanced Light Source) in Berkeley[32,33] has been benchmarked with theoretical calculations in LS coupling.[34] However, determination of its abundance has remained an unsolved problem because of the large discrepancy between the abundances calculated from collisional excitation and from recombination processes.

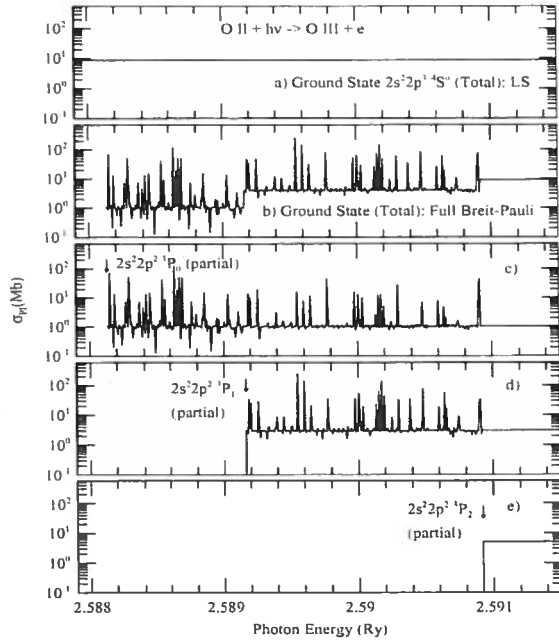Our latest calculations including relativistic fine

Fig. 10. Fine structure effects on ground state photoionization ($^4S^o$) of O II in low energy region.[7] a) σ_{PI}(LS) is a smooth line,[36] b) total σ_{PI} in relativistic Breit-Pauli showing resonances not allowed in LS coulpling. c,d,e) Partial photoionization cross sections ionizing in to levels $^3P_0$, $^3P_1$, and $^3P_2$ of O III.

Fig. 11. Photoionization cross sections σ_{PI} of the levels of ground configuration of O II, $^4S^o_{3/2}$ $^2D^0_{5/2,3/2}$ $^2P^o_{3/2,1/2}$, arranged in LS coupling approximation in the top panel followed below by those in fine structure.

structure for O II photoionization in the very low energy region near ionization threshold has revealed formation of crucial resonant structures by the fine structure couplings not seen before.[7] Fig. 10 shows σ_{PI} of $2s^22p^3(^4S^o_{3/2})$ ground state of O II in the low energy region.[7] The top panel shows σ_{PI} in LS coupling which is a smooth line without any feature.[36] But panel (b) presents total σ_{PI} from relativistic BPRM method where contributions of the full Breit-Pauli interaction has been included. The figure shows the resonant features as well as background jump at each core ionization threshold $^3P_0$, $^3P_1$, & $^3P_2$ of O III. Strong resonant structures below the core threshold ^4P state of $^5S^o$ state of Fe XXI were also found due to relativistic fine structure couplings and were seen in measured recombination spectra.[37]

These fine structure coupling effects in O II were not detected in the experiment[32,33] because of its narrow energy range. However, such near threshold resonances have now been found in a recent ALS measurement of σ_{PI} of Se II which has similar electronic configuration as O II.[38] Existence of these reso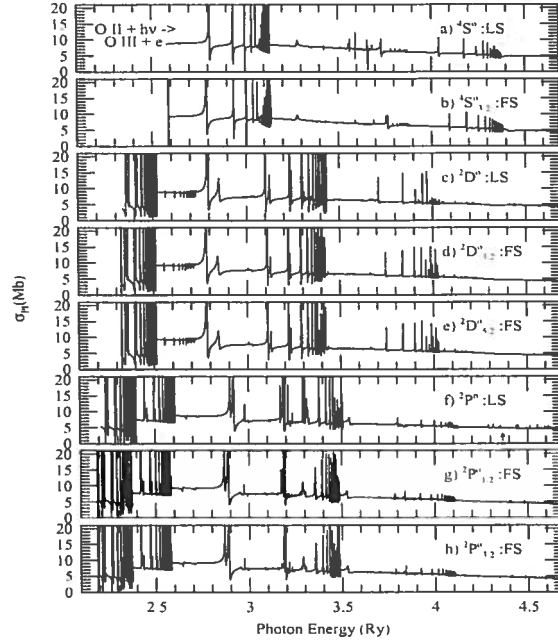nances were not explored also because of σ_{PI} in LS coupling similar to that in fine structure except at thresholds and hence showed good agreement with experiment.[32] Fig. 11 shows the cross sections of the three states of the ground configuration of O II, $2s^22p^3(^4S^o \, ^2D^o \, ^2P^o)$. In the figure, σ_{PI} in LS coupling is shown in a panel below which σ_{PI} in fine structure are shown. The comparison shows that the difference between LS coupling and fine structure cross sections is only right at the threshold where fine structure introduces resonance not seen in that in LS coupling.

The new resonant features at in energy σ_{PI} should narrow down the discrepancy of oxygen abundance in low temperature thin plasmas. Fig. 12 shows the recombination cross section from the low energy photoionization cross sections. The resonant structures when integrated over the Maxwellian distribution will increase the earlier rates at low temperature. This should bring the abundance close to that obtained from collision strength.
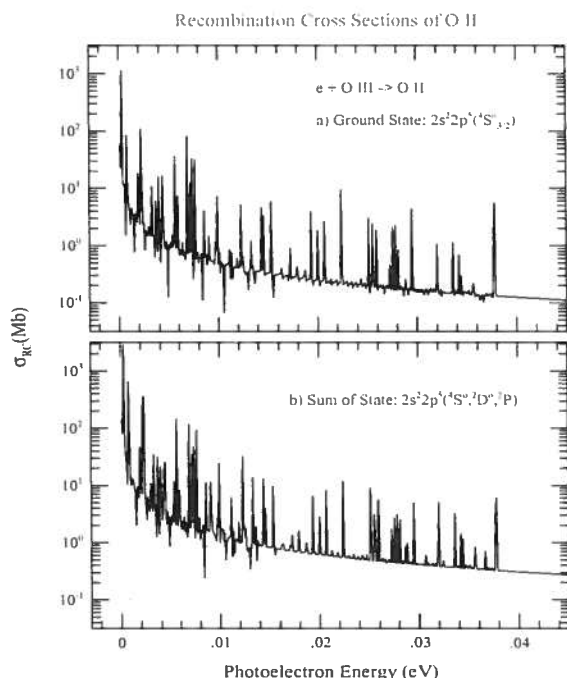
Fig. 12. Recombination cross section σ_{RC} of O II in the low energy region obtained (a) from the ground state and (b) from summed contributions of photoionization. The resonant structures at very low energy region, not found earlier, are due to fine structure couplings.

6. Conclusion

Accuracy of plasma opacities rely on the accurate atomic physics. Current opacities are not accurate enough to solve many crucial problems of astronomy, such as, solar elemental abundances are widely discordant. With the recent developments under the Iron Project, new results are indicating prospective solutions to the problems by consideration of accurate radiative transitions, relativistic fine structure effects, and photoionization resonances due to highly excited core states.

7. Acknowledgment

References

1. M.J. Seaton, *J. Phys.* B **20**, 6363 (1987)
2. The Opacity Project Team. *The Opacity Project*, Vol 1 (1995), Vol. 2 (1996) (Institute of Physics Publishing)
3. N.R. Simon, *ApJ* **260**, L87 (1982)
4. TOPbase: http://vizier.u-strasbg.fr/topbase/topbase.html
5. D.G. Hummer *et al.* *Astron. Astrophys* **279**, 298 (1993)
6. TIPbase http://cdsweb.u-strasbg.fr/tipbase/home.html
7. NORAD-Atomic-Data: www.astronomy.ohio-state.edu/~nahar/nahar_radiativeatomicdata/index.html
8. OPServer: http://opacities.osc.edu
9. K.A. Berrington *al. J. Phys.* B **20**, 6379 (1987)
10. K.A. Berrington *et al. Comput. Phys. Commun.* **92**, 290 (1995)
11. W. Eissner and G.X. Chen (*in preparation*, 2011)
12. S.N. Nahar, A.K. Pradhan, *Phys. Scr.* **61**, 675 (2000)
13. S.N. Nahar, *Astron. Astrophys. Suppl. Ser.* **127**, 253 (2000)
14. M. J. Seaton *et al., Mon. Not. R. Astron. Soc.* **266**, 805 (1994)
15. C.A. Iglesias and F.J. Rogers, *ApJ 371* **40**, 1991 (;) *ApJ* **464**, 943 (1996)
16. J.E. Bailey et al. (22 authors), *51st Annual meeting of the Division of Plasma Physics (DPP) of APS*, Atlanta, Georgia, November 2-6, 2009, TOc.010
17. *Atomic Astrophysics and Spectroscopy*, A.K. Pradhan and S.N. Nahar (Cambridge University Press, 2011)
18. W. Eissner, M, Jones, H. Nussbaumer, *Comput. Phys. Commun.* **8**, 270 (1974)
19. S.N. Nahar, W. Eissner, G.X. Chen, A.K. Pradhan, *Astron. and Astrophys.* **408**, 789 (2003)
20. S.N. Nahar, *Astron. Astrophys* **448**, 779 (2006)
21. S.N. Nahar, *Astron. Astrophys.* **457**, 721 (2006); Note- the published data at CDS were replaced later after a bug in R-matrix code was corrected.
22. S.N. Nahar, *At. Data. Nucl. Data.* (in press, 2011)
23. National Institute for Standards and Technology (NIST), compiled atomic data are available at *physics.nist.gov/PhysRefData/ASD/index.html*
24. T. Shirai *et al., J. Phys. Chem. Ref. Data* Monograph No.**8** (AIP Press), 632 pp. (2000)
25. K.T. Cheng, Y.K. Kim, and J.P. Desclaux, *At. Data Nucl. Data Tables* **24**, 111 (1979)
26. B.C. Fawcett, *At. Data Nucl. Data Tables* **31**, 495 (1984) DD
27. J.P. Buchet *et al., Phys.Rev.* A **22**, 2061 (1980)
28. S.N. Nahar and A.K. Pradhan, *Astron. Astrophys* **437**, 345 (2005)
29. S.N. Nahar, *J. Quant. Spec. Rad. Transfer* **109**, 2417 (2008)
30. S.N. Nahar, A.K. Pradhan, G.X. Chen, W. Eissner, (submitted 2011)
31. Y. Yu and M.J. Seaton, *J. Phys.* B **20**, 6409 (198)
32. A.M. Covington *et al., Phys. Rev. Lett* **87**, 243002-1 (2001)
33. H. Kjeldsen *et al., Astrophys. J. Suppl. Ser.* **138**, 219 (2002)
34. S.N. Nahar, *Phys. Rev.* A **69**, 042714-1 (2004)

35. S.N. Nahar, M. Montenegro, W. Eissner, A.K. Prad-
    han, *Phys. Rev.* A Brief Report **82**, 065401 (2010)
36. S.N. Nahar, *Phys. Rev.* A **58**, 3766 (1998)
37. S.N. Nahar, *J. Quant. Spec. Rad. Transfer* **109**,
    2731 (2008)
38. N. C. Sterling et al. (14 authors), *Publications of the
    Astron. Soc. Australia* **26**, 339 (2009)